Optics and Lasers in Engineering 122 (2019) 37–47

Contents lists available at ScienceDirect

Optics and Lasers in Engineering

journal homepage: www.elsevier.com/locate/optlaseng

# 2500-Channel single-shot areal profilometer using hyperspectral interferometry with a pinhole array

Tobias V. Reichold*, Pablo D. Ruiz, Jonathan M. Huntley

*Loughborough University, Wolfson School of Mechanical, Electrical and Manufacturing Engineering, Loughborough LE11 3TU, UK*

ARTICLE INFO

*OCIS codes:*
120.3930
100.3175
120.6650
110.5086

*Keywords:*
Metrological instrumentation
Interferometric imaging
Surface measurements
Phase unwrapping
Pinhole array
Hyperspectral

ABSTRACT

Surface profilometry techniques such as coherent scanning interferometry or focus variation require long scan times and are thus vulnerable to environmental disturbance. Hyperspectral interferometry (HSI) overcomes the problem by recording all the spatial and spectral information necessary to reconstruct a 2D surface height map in a single shot. In this paper, we present a new HSI system that uses a pinhole array to provide the necessary gaps for the spectral information. It is capable of measuring 2500 independent points, twice the previous maximum number, with a maximum unambiguous depth range of ~825 μm and a larger maximum surface tilt angle of 33.3 mrad. The use of phase information allows height to be measured to a precision of ~6 nm, an order of magnitude improvement on previous HSI systems.

## 1. Introduction

A wide range of contact and non-contact techniques now exist to measure absolute surface profiles and roughness. Contact tools such as drag stylus profilers or atomic force microscopy can make measurements irrespective of material composition, are able to cope with modest surface discontinuities and provide axial resolutions down to a few picometers [1]. However, the resultant force on the sample may change its shape or cause surface damage [1,2]. With scanning times per line as long as several minutes, measurements are also vulnerable to environmental disturbances such as temperature and humidity changes or ambient vibrations [3]. Areal scans comprising several line scans take correspondingly longer and are thus even more vulnerable to such influences.

Optical surface profilers based on coherence scanning interferometry (CSI) or focus variation avoid some of the problems of contacting instruments, and as a result are finding widespread industrial application [4]. In CSI, a Mirau or Michelson objective with a broadband source is used to scan a sample in the axial direction, the height of a given point on the sample being determined from the point of maximum fringe modulation at the corresponding camera pixel. The broadband nature of CSI allows absolute height measurements of surface steps without phase unwrapping, which would not be possible with monochromatic sources. However mechanical scanning components increase the required acquisition time, hence the sensitivity to environmental disturbances is high [5]. Single shot measurement approaches are required to remove environmental sensitivities, such as the system proposed by Schwider and Zhou in which a broadband Fizeau interferometer and grating spectrometer were used to measure absolute 1D line profiles [6].

A recent technique known as hyperspectral interferometry (HSI) eliminates the need for any mechanical movement, enabling single-shot areal measurements with low environmental sensitivity. As with CSI, the use of a broadband source removes the depth ambiguity that would be present when measuring discontinuous surfaces with a monochromatic source. A Linnik-type interferometer and a hyperspectral imager are used to spatially separate a set of narrowband interferograms on a 2D photodetector array (PDA) enabling 2D unambiguous optical path difference measurements in a single shot [7,8]. In the original proof of concept [7], an interference filter (etalon) was used to turn the broadband spectrum from a super luminescent diode (SLED) into a frequency comb that illuminates the object and a reference mirror. The object was imaged through the interferometer onto the PDA, while a diffraction grating at the pupil plane of the imaging optics redirected the narrowband interferograms that correspond to each peak of the frequency comb to distinct positions onto the PDA, along the grating's dispersion axis. Early implementations of HSI yielded a modest number of independent height measurements (~200), an unambiguous depth range of 350 μm and a depth measurement precision of 80 nm [7, 8]. Due to the etalon,

* Corresponding author.
*E-mail address:* t.reichold@lboro.ac.uk (T.V. Reichold).

https://doi.org/10.1016/j.optlaseng.2019.05.015
Received 7 March 2019; Received in revised form 7 May 2019; Accepted 14 May 2019
Available online 25 May 2019

optical throughout was compromised to ~1/15 of the input power and pixel utilisation was only ~2% of the available PDA.

A more efficient implementation of HSI utilised a microlens array (MLA) to significantly increase the number of independent measurement channels [9]. The MLA was placed at the output of an imaging Linnik interferometer at an intermediate plane where the object is imaged with some magnification, effectively spatially sampling the object and the reference mirror. At the focal plane of the MLA, an array of spots appears, each spot being an image of the pupil of the main imaging optics by one of the microlenses. An imaging spectrometer based on a diffraction grating then turns this set of spots onto an array of linear spectra on the PDA. A small rotation between the MLA and the dispersion axis of the grating was introduced to prevent overlap between spectra. The MLA-based HSI system provided 1225 channels (>6× more than the etalon based system), 10× more optical throughput and an unambiguous depth range of 880 μm. However, the MLA acts effectively as a Shack-Hartmann sensor and when the wavefront of the object beam reaches it at an angle (due to local surface slope) the corresponding spot at the MLA focal plane drifts from the spot produced by the reference beam and thus the interference is lost. This means that an MLA-based system can only deal with relatively small surface height gradients.

In the current paper, this shortcoming is addressed by means of an alternative way to spatially sample the interferometer output image. It is based on a pinhole array (PHA) similar to those used in lens-less in-line holographic microscopes [10] or more prominently in spinning Nipkow disk confocal microscopy [11]. Although the optical power throughput is reduced compared to an MLA-based system, a higher channel count and improved tolerance to large surface height gradients is achieved. In addition, the use of phase information is investigated for the first time in an HSI system, which is found to result in over one order of magnitude improvement in depth measurement precision. The paper is structured as follows: Section 2 describes the new proposed optical setup; Section 3 the experimental methodology to study the system performance; Section 4 presents experimental results for three different samples and a discussion and conclusions are offered in Section 5.

## 2. Experimental setup

The optical system is separated into two major subsystems: a balanced Linnik interferometer and a hyperspectral imaging system as shown in Fig. 1. The overall system is identical to the MLA-HSI predecessor as described in [9], except for the interface between the two

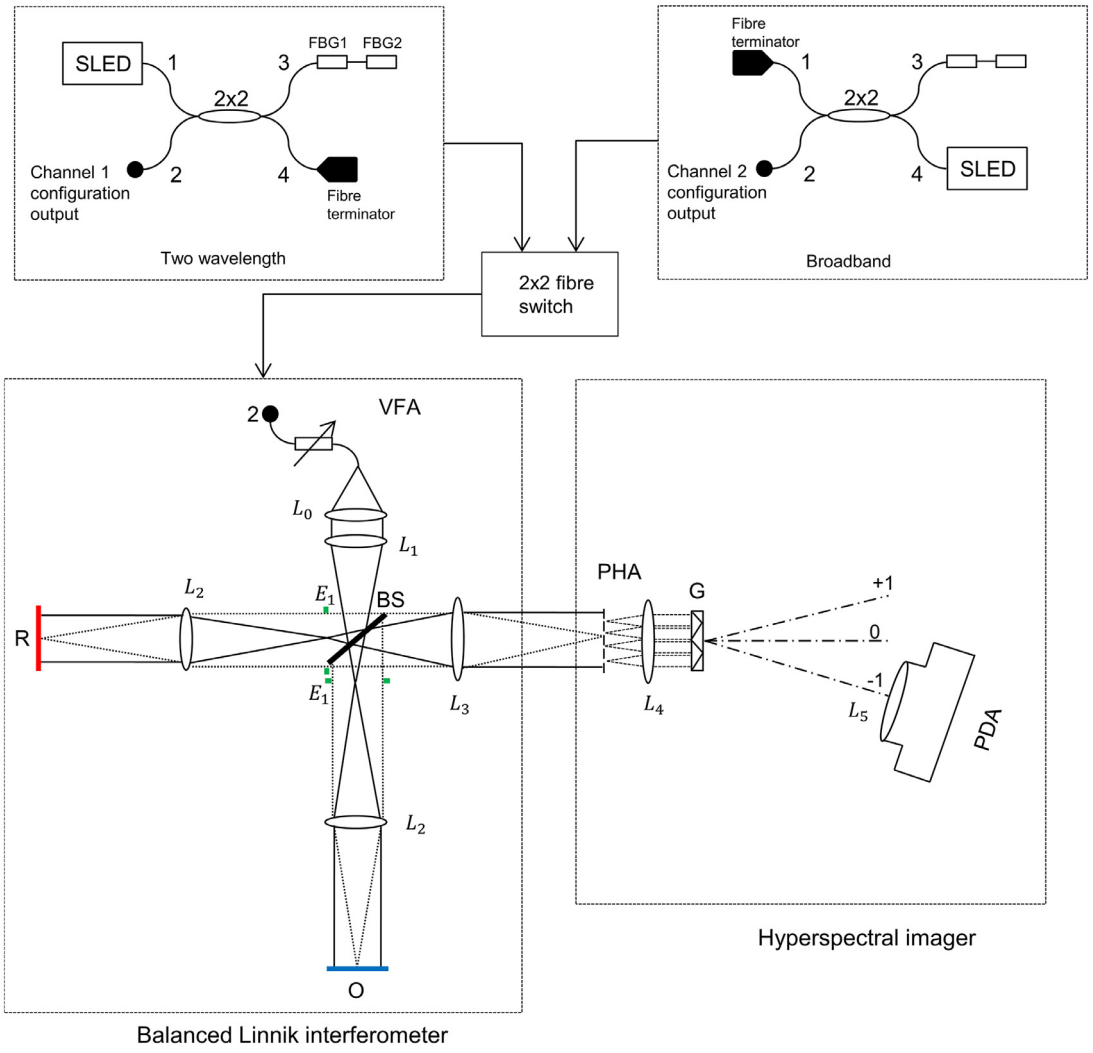


**Fig. 1.** Optical setup. The top part of the figure shows the two wavelengths illumination configuration used for spectral calibration and the broadband configuration used for absolute height measurements. The bottom diagram shows the interferometer and spectrometer subsystems. The main system components are: Superluminescent diode, SLED; 2 × 2 90:10 fibre coupler; fibre Bragg gratings FGB1 and FBG2; variable fibre attenuator, VFA; collimator lens $L_0$; Lenses $L_1$, $L_2$, $L_3$; Beam splitter, BS; reference mirror, R; object surface, O; pinhole array, PHA; imaging lenses $L_4$, $L_5$; transmission diffraction grating, G; and photodetector array, PDA.

subsystems: the object is imaged here onto an array of pinholes rather than microlenses. The hyperspectral imager in turn images the pinholes rather than the spots of light behind the microlenses. Provided the pinhole size is comparable to the spot size, the PHA-HSI therefore shares many of the same design considerations as the MLA-HSI.

### 2.1. Light source and interferometer

The interferometer's main light source is a super-luminescent diode (SLED, Superlum S840-HP1 15 mW) with a centre wavelength $\lambda_c = 840$ nm and a bandwidth $\Delta\lambda = 50$ nm at full-width-half-maximum (FWHM). A 90:10 2×2 single mode fibre coupler provides a two-state output for two independent illumination states. State one provides a "two wavelength" illumination condition by means of two series fibre Bragg gratings FBG1 and FBG2. This provides two selectively-filtered wavelengths $\lambda_1 = 820$ nm and $\lambda_2 = 853$ nm with a narrow spectral band < 0.01 nm for spectral calibration of the wavelength axis in the spectral images as described in [9]. State two provides a broadband illumination condition by coupling the SLED output directly into the interferometer launch optics. A variable fibre attenuator (OZ optics neutral density for SM 780HP fibre) is used to adjust the input power to avoid saturating the PDA for any given exposure time.

At the launch arm of the Linnik interferometer, singlet lens $L_0$ (100 mm focal length) collimates the expanded beam, while lenses $L_1$ and $L_2$ in both arms (150 mm focal length) are near-infrared (NIR) achromatic doublets set to illuminate the reference mirror and the object surface with collimated beams. BS is a 50:50 non-polarizing beam-splitter cube. $L_2$ in the reference and object arms and $L_3$ (150 mm focal length) at the recombination arm form bi-telecentric systems that image the reference mirror and the object at the back focal plane of $L_4$. At that plane, an image of the object interferes with the collimated reference beam so as to form a broadband interferogram [9].

### 2.2. Hyperspectral imager

A pinhole array on a chromium plated glass (50×50 pinholes, square grid, 10 μm pinhole diameter, 120 μm pitch) is used to spatially sample the superimposed images of the object and reference mirror. The effective field of view is 5.88 mm × 5.88 mm. A given pinhole labelled by indices ($m$, $n$) collects light from a small region on the sample surface, centred on a point with coordinates ($x_m$, $y_n$), where $m = 0, 1, 2, \ldots, N_x - 1$; $n = 0, 1, 2, \ldots, N_y - 1$ and $N_x$, $N_y$ are respectively the number of pinholes along the $x$ and $y$ axes [9].

The pinholes are imaged onto a photodetector array (PDA, Apogee U16M, 4096 × 4096 pixels, pixel size 9 μm, array size 36.86 mm array diagonal 52.13 mm) with imaging lenses $L_4$ (Nikkor 50 mm f/# 1.8) and $L_5$ (Nikkor 135 mm f/# 2.8). A blazed near-infrared diffraction grating G (300 lines $mm^{-1}$) diffracts the collimated beams that $L_4$ produces for each pinhole, thus creating a 1-D spectral signal that fits between the images of neighbouring pinholes. The −1 diffraction order has the highest intensity for this grating and is captured by $L_5$ to image an array of spectra onto the PDA. The magnification $m_{54}$ for lenses $L_4$ and $L_5$ is equal to 2.709 (as measured using the known pinhole pitch and the distance between pinhole images on the PDA), which in combination with the 300 lines $mm^{-1}$ diffraction grating result in an individual spectrum length of approximately 2.093 mm on the PDA. Therefore, a maximum of ~234 pixels are available for each spectrum.

### 2.3. Spatial encoding of spectral information

The spatial encoding of spectral information is identical to that for a MLA. The key points from [9] are summarized here to aid comprehension of the concept.

Fig. 2(a) shows a schematic view of an object that has a surface step which is imaged onto the PHA (Fig. 2(b)). Both the coordinate system of the sample, and the row/column axes of the PHA, are rotated by a small angle $\alpha$ with respect to the row/column axes of the PDA to avoid cross-talk and spectral leakage of adjacent spectra. A PHA with reduced number of pinholes ($N_x = N_y = 5$) is used in Fig. 2(b) to illustrate the concept.

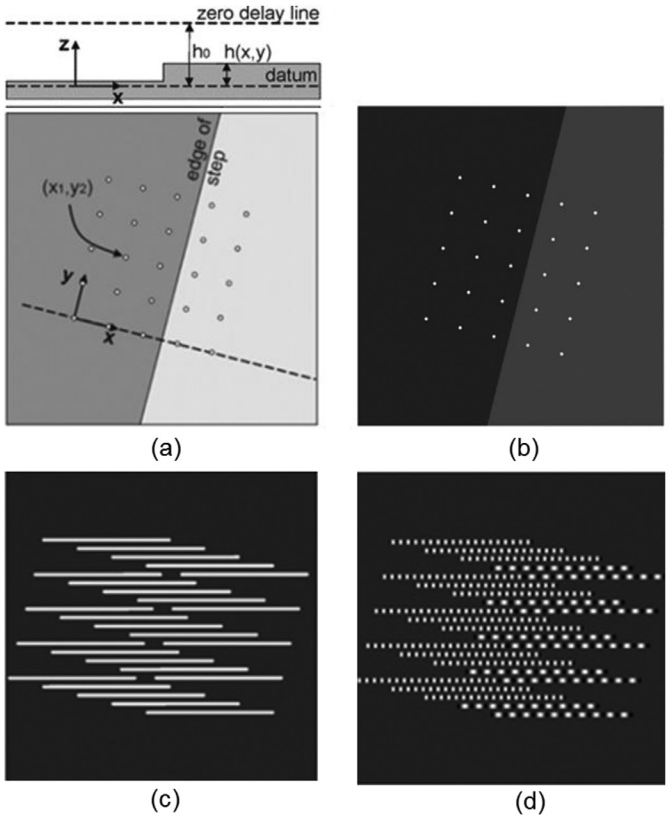


**Fig. 2.** Encoding of surface height in pinhole-array-based hyperspectral interferometer: (a) object with a surface step profile. The insert above shows a cross-section through the sample with height distribution $h(x, y)$. Lines indicating cross-sections through the zero optical path difference and sample datum surfaces are also shown; (b) image of the object on the pinhole array; (c) array of spectra (no reference beam in the interferometer); (d) spectra (shown here in monochrome for clarity) are modulated by fringes which frequency encode surface height from datum (adapted from [9]).

Provided the diffraction grating G in Fig. 1 is set with the grooves parallel to the columns of the PDA array, the spectra align parallel to the rows. Fig. 2(c) illustrates the spectra when only one of the reference or object beams is imaged onto the MLA. When both beams are present on the MLA (Fig. 2(d)), the spectra are modulated with fringes with a spatial frequency that encodes the optical path difference between the object and reference beams for the corresponding pinhole in the PHA. We denote the sampling points along the wavenumber axis by $k_p$ where $p = 0, 1, 2, \ldots, N_k - 1$, and $N_k$ is the total number of sample points.

### 2.4. Reduced sensitivity to sample tilt

A drawback of the previously-proposed MLA-based system [9] is that its performance deteriorates when imaging a specularly-reflecting sample whose normal is misaligned with respect to the optical axis of $L_2$. As stated previously this is because the rays from the tilted surface enter each microlens at a finite angle causing the focused spots to shift sideways. This is shown schematically in Fig. 3(a) for a single microlens, together with the intensity cross section through the microlens's point spread function.

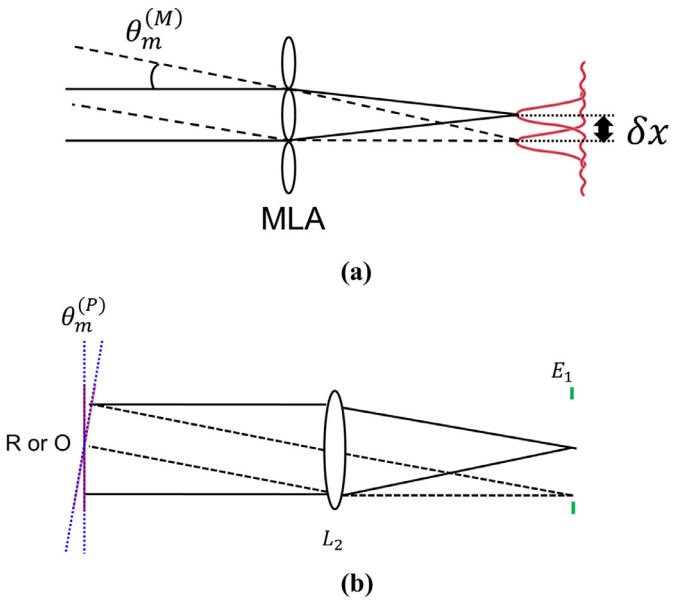


**Fig. 3.** Susceptibility of (a) MLA- and (b) PHA-based HSI systems to sample tilt for the case of smooth (non-speckled) wavefronts.

If $\theta_m^{(M)}$ represents the angle between the surface normal and optical axis of $L_3$, the lateral shift of the spot is

$$\delta x = 2\theta_m^{(M)} f_3 \tag{1}$$

where $f_3$ is the focal length of a microlens. Interference signal is therefore lost when $\delta x$ equals or exceeds the diameter of the point spread function (PSF) of the imaging system, given by

$$d_{PSF3} = \frac{1.22\lambda_c}{NA_3}, \tag{2}$$

where $\lambda_c$ is the central wavelength and $NA_3$ is the numerical aperture of the microlenses. The maximum allowable surface slope angle for a MLA-based system, $\theta_m^{(M)}$, follows from Eqs. (1) and (2) as:

$$\theta_m^{(M)} = \frac{0.61\lambda_c}{f_3 NA_3} \approx \frac{1.22\lambda_c}{D_3}, \tag{3}$$

where $D_3 = 100$ μm is the microlens diameter.

The situation for the PHA-based HSI system, on the other hand, is different because the pinhole locations are fixed. So long as light reaches a given pinhole from the sample, interference with the reference beam will always occur. The limitation on tilt angle is now given by the requirement that light from the sample passes through aperture $E_1$. Tilt or surface slope in the object causes the focused spot at $E_1$ to move in the plane of the circular aperture. Loss of signal occurs when this spot moves laterally by a distance $\frac{D_1}{2}$ from the centre position, where $D_1 = 20$ mm is the diameter of $E_1$. This corresponds to a maximum permissible surface slope angle

$$\theta_m^{(P)} = \frac{D_1}{4f_2}, \tag{4}$$

where $f_2$ is the focal length of lens $L_2$. For the systems described in this paper and [9], $\theta_m^{(P)}$ and $\theta_m^{(M)}$ take the values 33.33 mrad and 10.24 mrad, respectively; the use of the PHA therefore results in an increase in allowable tilt by approximately 3.25×.

## 3. Data analysis

### 3.1. 'Standard' HSI analysis

Each pinhole produces a 1-D spectral intensity signal in the same way as each microlens in the previous MLA set-up [9]. Identical signal processing procedures are therefore applicable. After removal of the *DC* term, each interferogram is multiplied by a Hanning window and Fourier transformed. An iterative bounded Newton-Raphson method is used to locate the Fourier peak from each interferogram. At the peak, frequency and phase information is recorded and the frequency is converted to optical path difference, $z_0$, using the following equation:

$$z_0(m,n) = (2\pi/\Delta k) f_k(m,n), \tag{5}$$

$f_k$ is the frequency in units of cycles across the spectral bandwidth used, $\Delta k = k_2 - k_1$, where $k_1$ and $k_2$ are the minimum and maximum wavenumbers respectively [9]. The 'two wavelength' measurement provides the scaling factor that allows pixel location to be converted to wavenumber. $z_0$ can be considered as an estimate of the OPD, which is related to the surface height value as:

$$z_0(m,n) = 2\left[h_0 - h(m,n)\right]. \tag{6}$$

$h_0$ is the known distance from the sample datum surface to the plane of zero optical path difference, as shown in Fig. 2(a).

### 3.2. HSI analysis using phase information

HSI implementations so far have used only the frequency of the recorded fringes to infer depth. The phase of the interference signal, as determined from the argument of the Fourier transform peak, has previously been ignored. By contrast, phase in CSI has been used for many years to provide lower-noise estimates of OPD [12]. A general algorithm to estimate OPD from the phase at the transform peak, using intensity measured as a function of wavenumber, has been proposed recently [13] and we therefore investigate its applicability to HSI data. $\phi_1$ will be used to denoted the phase calculated from the real and imaginary parts of the transform at the positive frequency peak corresponding to OPD = $z_0$. It can be shown that $\phi_1$ is a sum of two terms:

$$\phi_1 = \phi_0 + k_1 z_0 \tag{7}$$

$\phi_0$ is a phase offset that arises due to the relative phase shifts on reflection from the object and the reference mirror. The second term arises from the fact that the interference signal is shifted by $-k_1$ along the wavenumber axis prior to Fourier transformation. By the Fourier shift theorem, this gives rise to an additional factor $\exp(ik_1 z_0)$ at the Fourier peak at OPD = $z_0$.

A single phase measurement is insufficient to separate the $\phi_0$ and $k_1 z_0$ terms from Eq. (7). If $\phi_0$ is not known *a priori*, for example from documented material properties or a previous calibration, it can be estimated in a least squares sense from data taken from a region of the sample known to have a constant value of $\phi_0$ [13]. Such an estimator for $\phi_0$ will be denoted $\hat{\phi}_0$, with the estimators for $z_0$ provided by Fourier peak location and phase denoted by $\hat{z}_0^{(1)}$ and $\hat{z}_0^{(2)}$, respectively. $\phi_1 - \hat{\phi}_0$ is a wrapped phase, lying in the range $-\pi$ to $\pi$, but can be unwrapped by using the phase $k_1\hat{z}_0^{(1)}$ to give the phase estimator for $z_0$:

$$\hat{z}_0^{(2)} = \frac{1}{k_1}\left[\phi_1 - \hat{\phi}_0 - 2\pi\, NINT\left(\frac{\phi_1 - \hat{\phi}_0 - k_1\hat{z}_0^{(1)}}{2\pi}\right)\right] \tag{8}$$

where *NINT* is a function that rounds to the nearest integer. The map of OPD resulting from applying Eq. (8) to the fringe pattern from each of the pinholes can then be converted into a height map using Eq. (6). The performance of these two approaches is compared experimentally in the next section.

## 4. Experimental results

The system was tested with three different object configurations, as shown in Fig. 4. Every time a new sample was loaded into the object arm of the interferometer, its surface was brought to the plane of zero optical path difference with the reference beam (which we refer to here as zero delay line, ZDL) by means of a translation stage. As the object

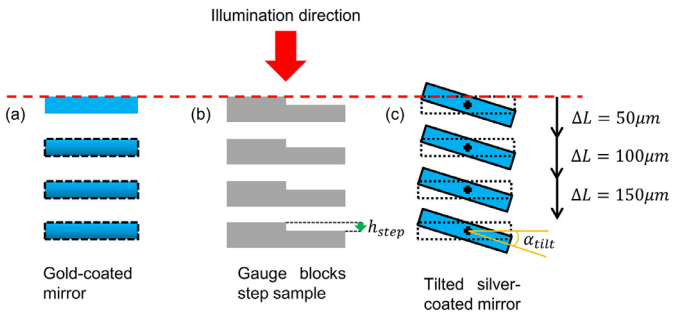


**Fig. 4.** Different object configurations viewed from above. The red dashed line is a cross section through the Zero Delay Line surface.

moves towards the ZDL, the spatial frequency of the spectral fringes is gradually reduced and it approaches 0 at the ZDL location. Fringes due to a global relative tilt between the object and reference mirror surfaces can also be observed (and compensated for) close to the ZDL. These appear across the whole object field of view because the chromium mask on the PHA is not fully opaque at near infrared wavelengths, and are convenient for the removal of any residual tilt against the reference beam.

Fig. 4(a) shows the case of a gold-coated mirror that was placed at four different positions relative to the ZDL. Fig. 4(b) shows a pair of gauge blocks with known height difference, which were used to assess the accuracy of step height measurements. Fig. 4(c) illustrates a silver coated mirror mounted on a PZT driven tilting stage (S-334.2SL, Physics Instruments, maximum mirror range ±50 mrad, repeatability = 5 μrad).

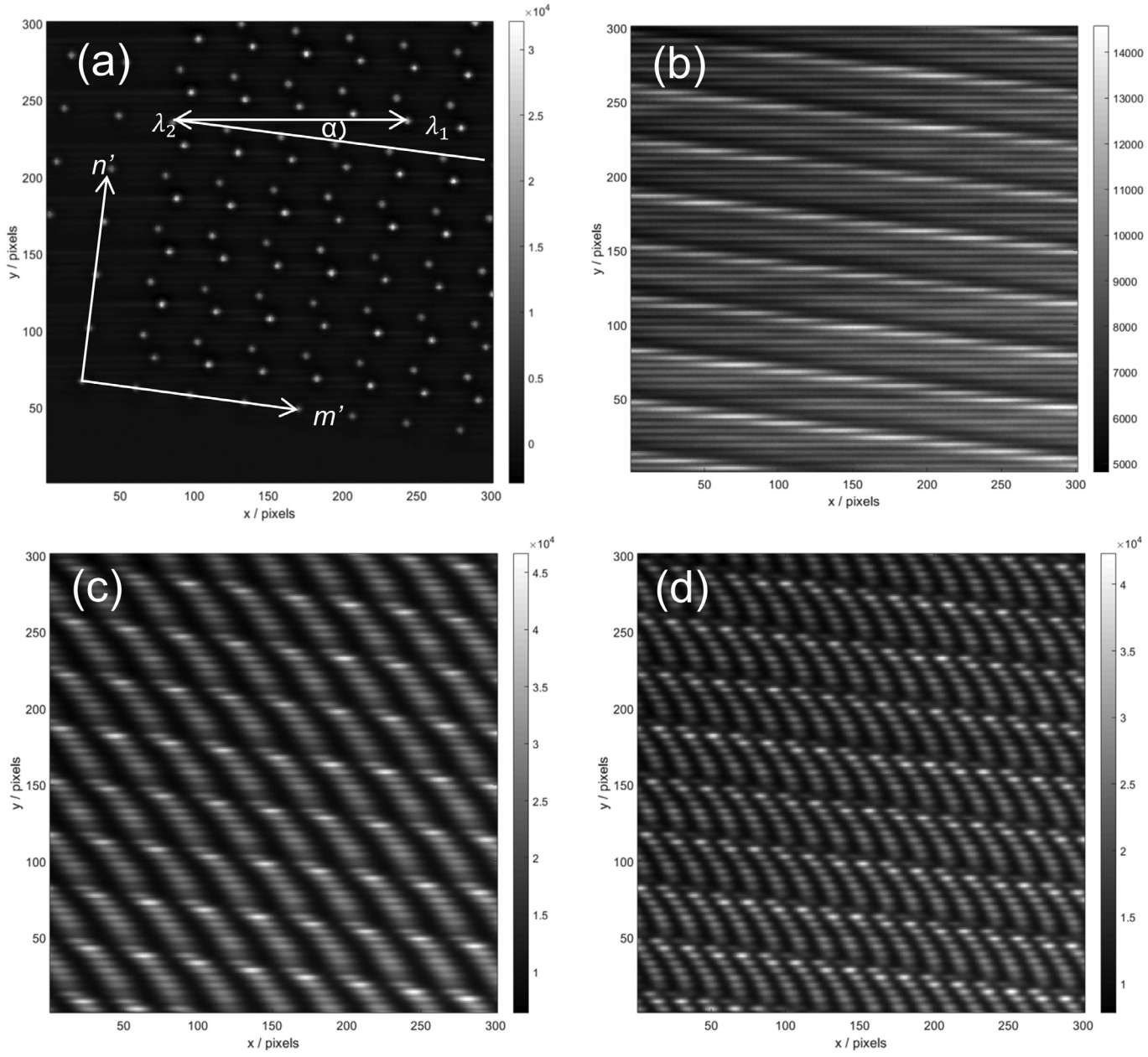


**Fig. 5.** Portion of an image of the PHA through the imaging spectrometer when a gold-coated flat mirror is observed using: (a) two-wavelengths illumination configuration and reference wave alone; (b) broadband illumination configuration and reference wave alone; (c) Broadband configuration with reference and object waves (mirror surface at 50 μm from the ZDL); (d) as (c) but with the mirror surface at 100 μm from the ZDL.

It can be tilted by a known angle $\alpha_{tilt}$ with respect to the optical axis to assess the performance of the system in terms of surface slope. Further details of these experiments are provided in Sections 4.2–4.4.

### 4.1. Two-wavelength illumination

Using the two-wavelengths illumination configuration, an image is taken with light from the reference or object arm alone. Each pinhole in the array produces two spots, as shown in Fig. 5(a). The horizontal arrowed line indicates the image locations of a single pinhole at the two wavelengths $\lambda_1$ and $\lambda_2$. The $m$' and $n$' axes are parallel to the $m$ and $n$ axes, respectively, but with an arbitrary shift between the two coordinate system origins, and demonstrate the rotation of the PHA with respect to the PDA. This image is used for the calibration of the wavelength axis for the later spectral images using the same procedure as described in [9]. As the grating equation is non-linear the distance $d$ between the $\lambda_1$ and $\lambda_2$ pinhole images vary slightly with pinhole indices as shown in Fig. 6.

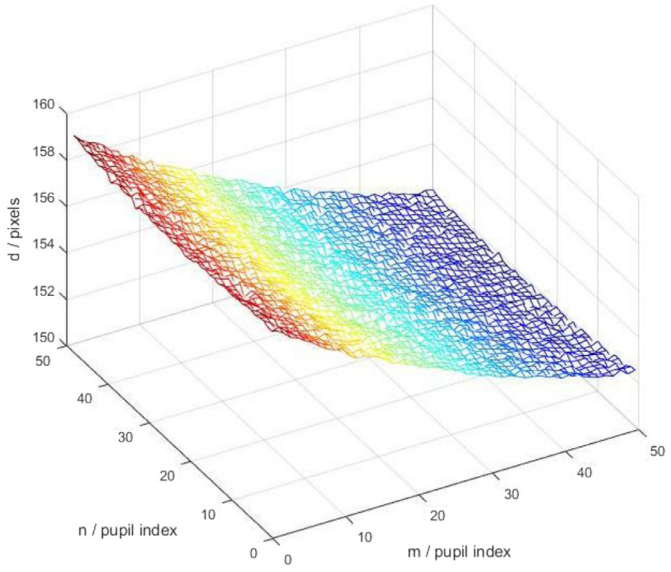


**Fig. 6.** Separation between the spots corresponding to $\lambda_1$ and $\lambda_2$ pinhole images for each of the 50 × 50 pinholes.

### 4.2. Broadband illumination – gold-coated mirror

A gold-coated mirror mounted on a translation stage was used as the first object. This allowed the noise level in the measurements to be estimated at a range of distances from the ZDL. Using broadband illumination, two images were taken: one with the reference wave, the other with the object wave. This provided the spectrum of each of the two waves and hence allowed the DC and low-frequency terms in the interference signal to be fully removed for subsequent single-shot imaging [9]. A series of interferograms was then taken at 50 μm steps from the ZDL location as shown schematically in Fig. 4(a). With increasing OPD, the modulation frequency of the individual spectra increases as shown in Fig. 5(c) and (d). The horizontal profile through the fringe modulated spectrum corresponding to the centre pinhole when the mirror was at 100 μm from ZDL is shown in Fig. 7(a). The DC term was first removed, then the signal was normalised to remove the influence of the source

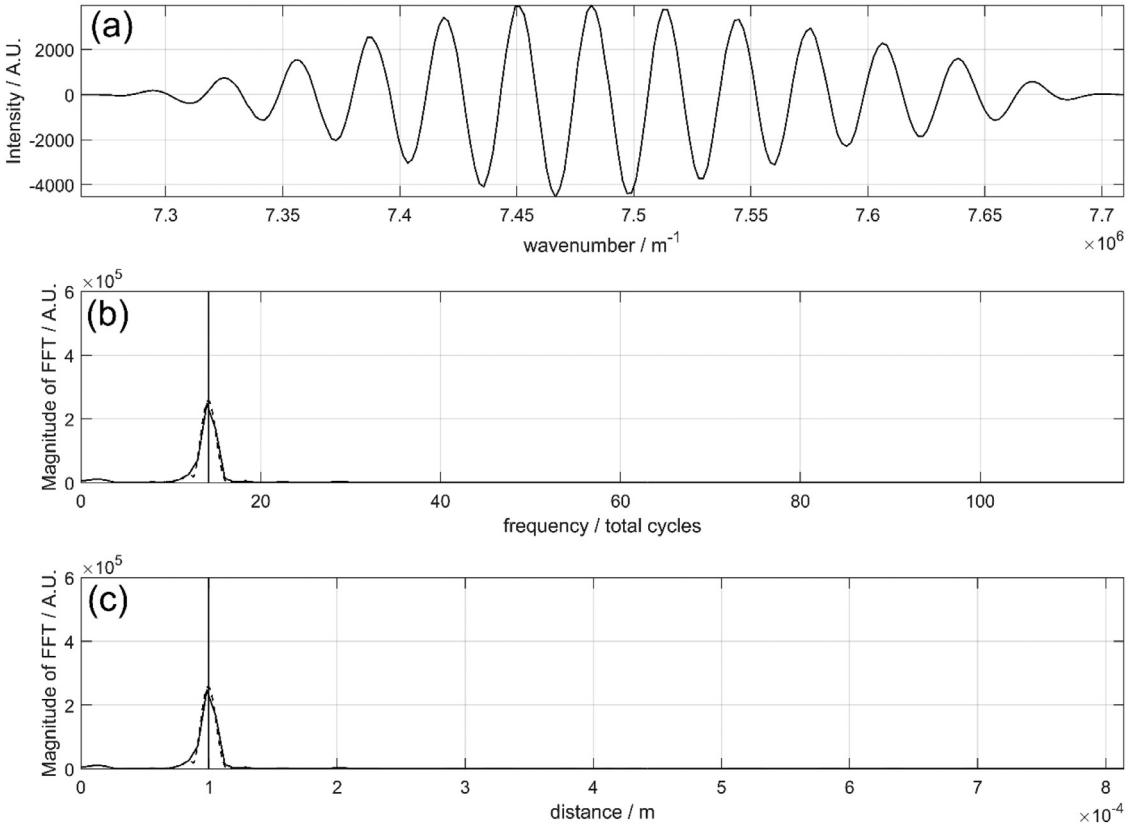


**Fig. 7.** Interferogram corresponding to the central pinhole when the mirror is at 100 μm from the ZDL: (a) Intensity profile vs wavenumber after DC subtraction, spectral normalisation and application of a Hanning window; (b) Magnitude of the Fourier transform of (a); (c) Same as (b) but with horizontal axis scaled to distance from ZDL.

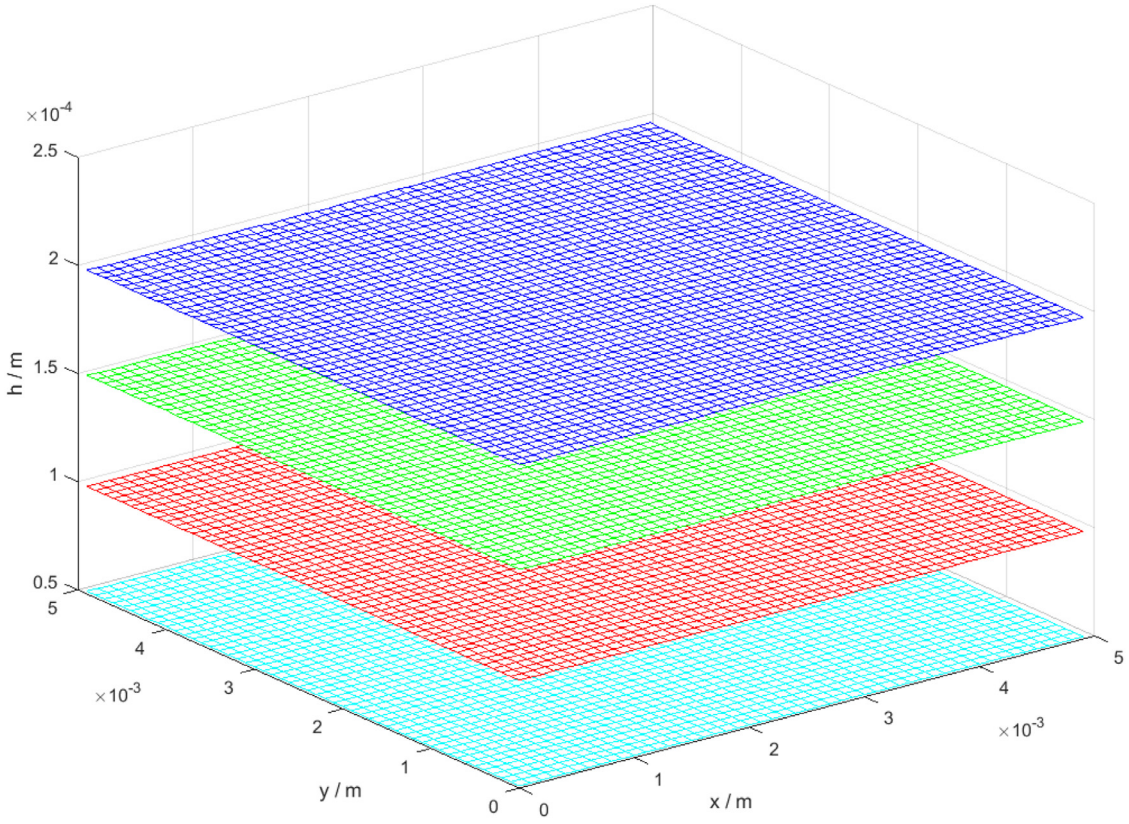


**Fig. 8.** Stacked height maps of a flat gold coated mirror moved axially with a translation stage in 50 μm steps at 50, 100, 150 and 200 μm, respectively.

**Table 1**
Rms residual values in nm for flat gold-coated mirror at three locations relative to ZDL position.

| Analysis method | Polynomial degree | $\Delta h$ =50 μm | $\Delta h$ =100 μm | $\Delta h$ =150 μm | $\Delta h$ =200 μm |
|---|---|---|---|---|---|
| Peak location | 1 | 122 | 141 | 157 | 222 |
| Peak location | 2 | 95.4 | 123 | 141 | 213 |
| Phase | 2 | 5.8 | 7.9 | 10.1 | 12.6 |

spectral envelope, and finally a Hanning window was applied along the wavenumber axis to reduce spectral leakage [9]. The Fourier transform contains a dominant peak, the position of which indicates the distance from the mirror surface to the ZDL, as described in Section 3.1.

Fig. 8 shows three 50 × 50 stacked height maps of the mirror at displacements $\Delta h$ = 50, 100 and 150 μm from the ZDL. Each map corresponds to a field of view of 5.89 × 5.89 mm$^2$. A total of 7500 independent coordinates were measured, 2500 for each surface map. The mean displacement measured by the system between the first and second locations (cyan and red surfaces, respectively) is 48.74 μm, 51.34 μm between the second and third locations (red and green surfaces) and 48.56 μm between the third and fourth locations (green and blue surfaces). These values are consistent with the nominal known displacement of 50 μm and a positioning accuracy of ~ 1 μm, corresponding to 1/10 of a division on the micrometer of the manually-driven translation stage.

The modulation of the spectral interference profile approaches zero outside the range $k = 7.709 \times 10^6 - 7.263 \times 10^6$ m$^{-1}$ which is equivalent to a wavelength range of 815–865 nm. This is the same as the specified bandwidth of the SLED source and is twice the wavelength range of the previously-described MLA system [9]. The spectral range 815–865 nm was sampled with 234 pixels, giving an effective inter-pixel increment in wavelength and wavenumber of $\delta\lambda = 0.21$ nm, and $\delta k = 1.904 \times 10^3$ m$^{-1}$, respectively. The corresponding theoretical height range $h_m = \frac{\pi}{2\delta k} = 0.825$ mm.

The measurement error of the system can be characterised by the root mean square (rms) residuals after least squares fitting of a polynomial surface to the data. The rms values for a first and second degree fit are shown in Table 1. The residuals from a 2nd degree polynomial fit, in the range 95–141 nm, are ~6× lower than corresponding values for the previously described MLA system [9].

Even lower residuals are produced by the phase analysis method. The extracted phase maps $\phi_1(m, n)$ for 50,100, 150 and 200 μm from ZDL are shown in Fig. 9. An average phase offset value $\hat{\phi}_0 = 0.897$ rad was calculated using the procedure described in [13]. The final height maps $h(m, n)$ produced after unwrapping using Eq. (8) are shown in Fig. 10. Some of the phase values for $\Delta h$ = 50 μm were not unwrapped correctly leading to anomalously high residual values and are not considered further here.

The height maps show relatively large deviations from flatness (rms residual of 438 and 509 nm with respect to a best-fit plane); as these are approximately 8× the known deviation from flatness for the mirror ($\lambda$/10 at 633 nm) they are likely to be an artefact of the sensor. One possible cause is a defocusing error: if lenses $L_1$ in the reference and object arms have a small axial position errors, the wavefronts arrive at the PHA with slightly different curvatures. The reproducible nature of this systematic error, apparent in the very similar profiles in Fig. 10 for the four different distances from ZDL position, means that it could in any case be removed by suitable calibration. The main feature of interest is the noise level. At 5.8 nm and 12.6 nm rms residual with

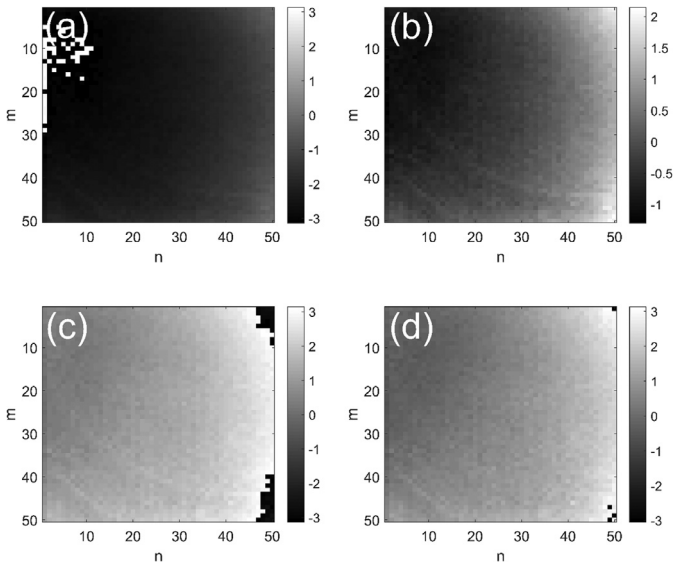


**Fig. 9.** Raw phase maps $\phi_1(m, n)$ before unwrapping for gold mirror sample at $\Delta h$ =50 µm (a), 100 µm (b), 150 µm (c), and 200 µm (d).

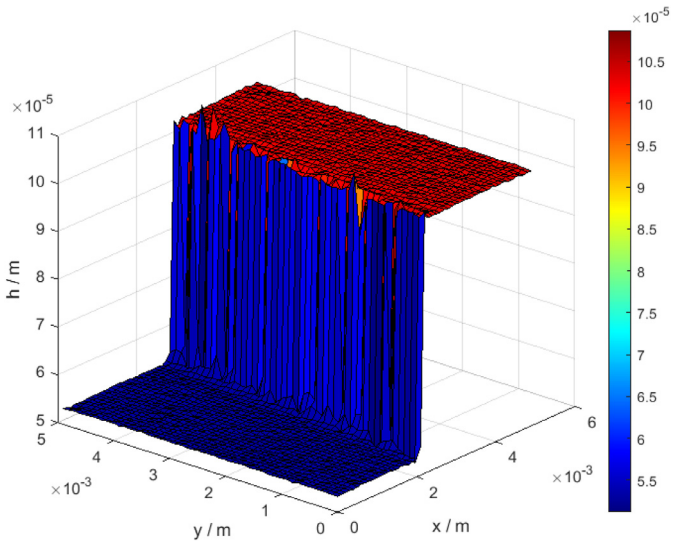


**Fig. 11.** Height map for gauge block step sample.

respect to a 2nd degree polynomial for the cases $\Delta h$ = 50 µm and 200 µm, respectively, this is over an order of magnitude lower than with the standard peak location analysis method.

### 4.3. Broadband illumination – height step

The second sample was made from calibration blocks so as to contain a well-defined surface step, as shown schematically in Fig. 4(b). The base block is a 30 mm × 34 mm × 9 mm gauge block onto which two smaller gauge blocks of dimensions 30 mm × 9 mm × 1 mm and 30 mm × 9 mm × 1.05 mm are wrung together. The average step height over the full step width was 49.765 $\mu$m ± 40 nm as determined with a TALYSURF CLI 2000 surface profiler.

Fig. 11 shows the measured areal profile over a 5 mm × 5 mm region straddling the step as measured using the peak location analysis method. As the PHA is rotated relative to the step edge, some of the pinholes

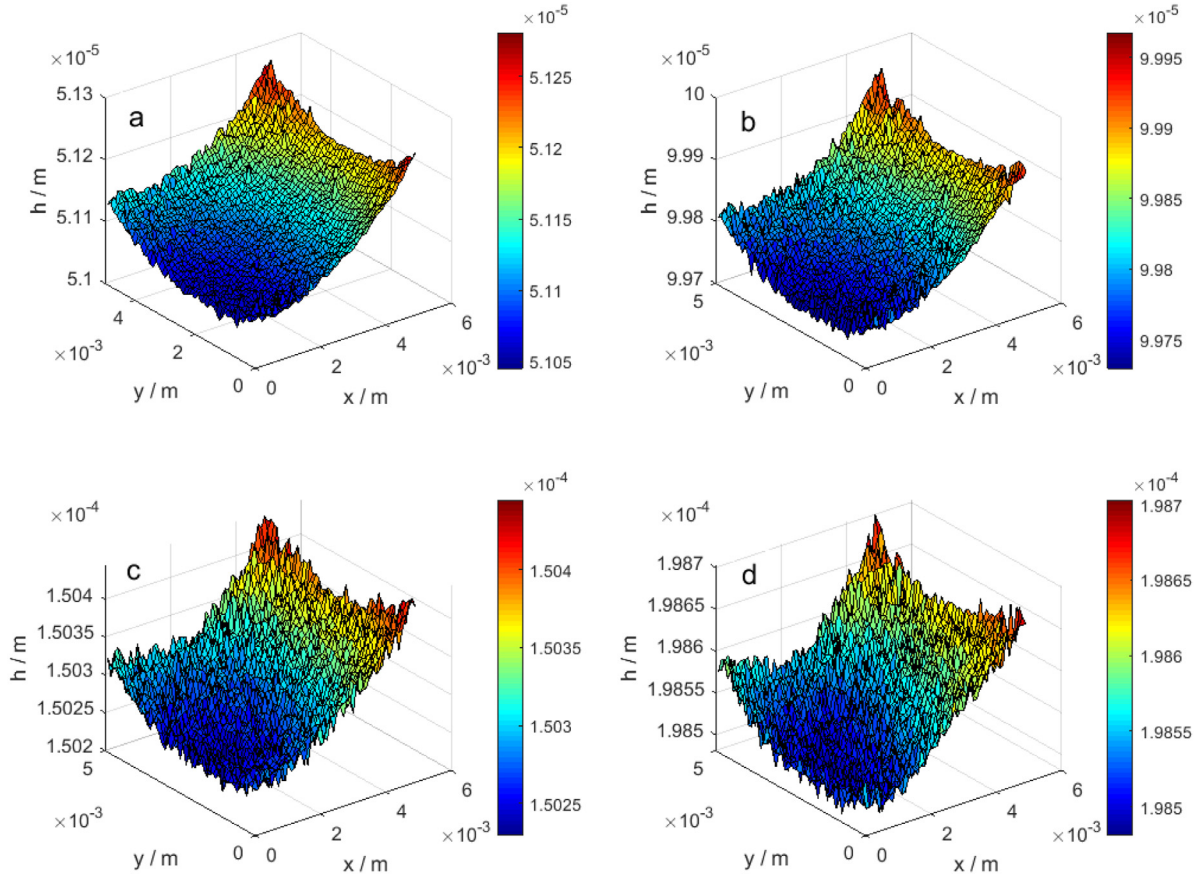


**Fig. 10.** Height maps $h(m, n)$ for gold mirror sample after phase unwrapping at (a) $\Delta h$ = 50 µm, (b) $\Delta h$ = 100 µm, (c) $\Delta h$ = 150 µm and (d) $\Delta h$ = 200 µm.

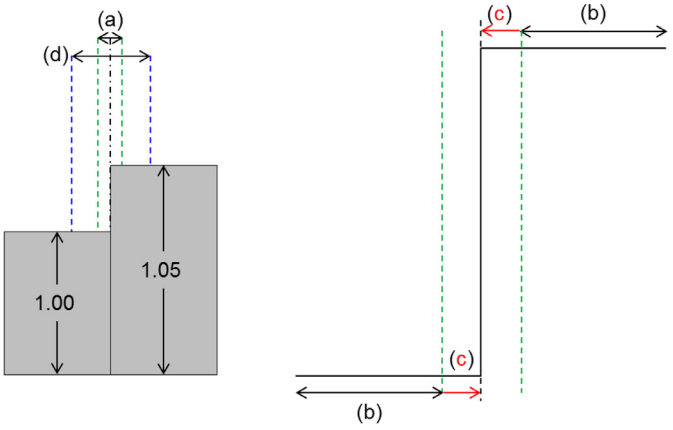


**Fig. 12.** Gauge block step sample setup shown from the side (left); close-up of region (d) with area of interest (a) around the step (right).

sample simultaneously parts of the top and bottom surface at the same time resulting in noisy data in that region.

In order to reduce the error in this region and obtain a good estimate of measured height on each side of the step, an extrapolation technique was used as shown in Fig. 12.

A region of interest around the diagonal transition line was bounded as indicated by the green dashed lines at position (a) in Fig. 12. The remaining parts of the top and bottom surfaces were fitted with 1st degree polynomials to reduce noise as indicated by zone (b). Finally, two-way extrapolation was performed which extrapolates the fitted top and bottom surfaces backwards and forwards respectively as indicated by zone (c), using the first degree best-fit polynomials, to obtain an estimate of the step height. Although higher degree polynomials could have been used as alternative extrapolating functions, a simple plane provided a good fit to the data on both sides of the step, and with a reduced number of parameters is less susceptible to noise-induced errors at the edges of the extrapolated region. The widths of each zone (a), (b), (c) were respectively 1 mm, 2 mm, 0.5 mm for both top and bottom surfaces. (d) is the sum of all (b) and (c). The average step height across the sample is $|h_{step}|$ = 49.78 μm with a maximum deviation of ± 57.03 nm for the case $\Delta h$ = 50 μm. Corresponding values for $\Delta h$ = 100 μm were $|h_{step}|$ = 49.92 μm ± 67.89 nm; and for $\Delta h$ = 150 μm, $|h_{step}|$ = 50.21 μm ± 83.73 nm. Note that this error refers to the variations in step height along the calculated transition line and does not represent the rms height error of the top or bottom surface which varied typically over the range 100–300 nm.

### 4.4. Broadband illumination – tilting surface

The third sample was a silver coated mirror mounted on a PZT driven tilting stage. The mirror rotates a known angle about an axis perpendicular to the optical axis. A tilted sample with 5 mrad nominal tilt using the tilting stage, at 50 μm from the ZDL, is shown in Fig. 13. A first degree fit was applied to the surface map and the unit surface normal vector was used to establish the surface tilt relative to a reference mirror pose also at 50 μm from ZDL with nominal 0 mrad tilt.

The 0 mrad reference plane shown in Fig. 13 (right, (b)) has a slightly negative tilt value if counter clockwise rotation is defined to be positive. The angular shift between any two planes can be calculated from the surface normals of the 1st degree fitted planes. The results for all tilt angles, relative to the measured 0 mrad reference plane, and at different offsets from the ZDL are shown in Table 2. Below $\theta$ = 10 mrad, the measurements between different offsets are consistent with one another to

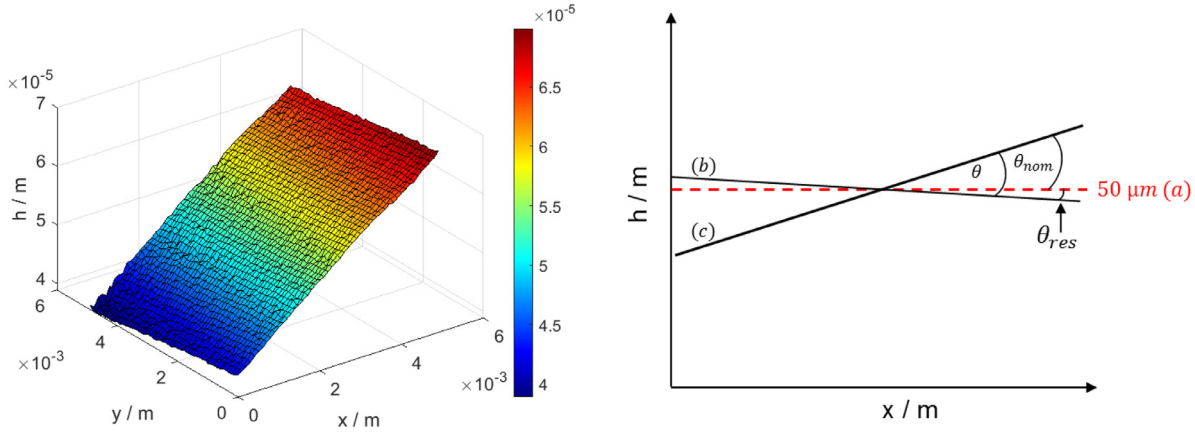


**Fig. 13.** Left: Measured height map for silver mirror at 5 mrad apparent tilt angle, 50 μm from ZDL location; Right: Schematic side view, XZ plane of measurement; (a) 0 mrad plane at 50 μm from ZDL, (b) measured 0 mrad with residual angle $\theta_{res}$ to (a), (c) is tilted surface plane with $\theta_{nom}$ = 5 mrad, $\theta$ is measured tilt angle relative to (b).

**Table 2**
Tilt sample rms height error, and calculated tilt angle $\theta$, for three offsets $\Delta h$ from zero OPD position.

| Nominal tilt angle / mrad | Rms height error / nm | | | Calculated tilt angle / mrad | | |
|---|---|---|---|---|---|---|
| | $\Delta h$ = 50 μm | $\Delta h$ = 100 μm | $\Delta h$ = 150 μm | $\Delta h$ = 50 μm | $\Delta h$ = 100 μm | $\Delta h$ = 150 μm |
| 1 | 161 | 147 | 163 | 0.80 | 0.78 | 0.74 |
| 2 | 151 | 164 | 154 | 2.11 | 2.08 | 1.99 |
| 3 | 180 | 184 | 191 | 3.61 | 3.61 | 3.59 |
| 4 | 212 | 178 | 188 | 4.14 | 4.18 | 4.22 |
| 5 | 282 | 185 | 192 | 5.58 | 5.57 | 5.44 |
| 10 | 628 | 273 | 340 | 11.81 | 11.82 | 11.80 |
| 15 | 615 | 1315 | 863 | 15.13 | 17.71 | 17.71 |

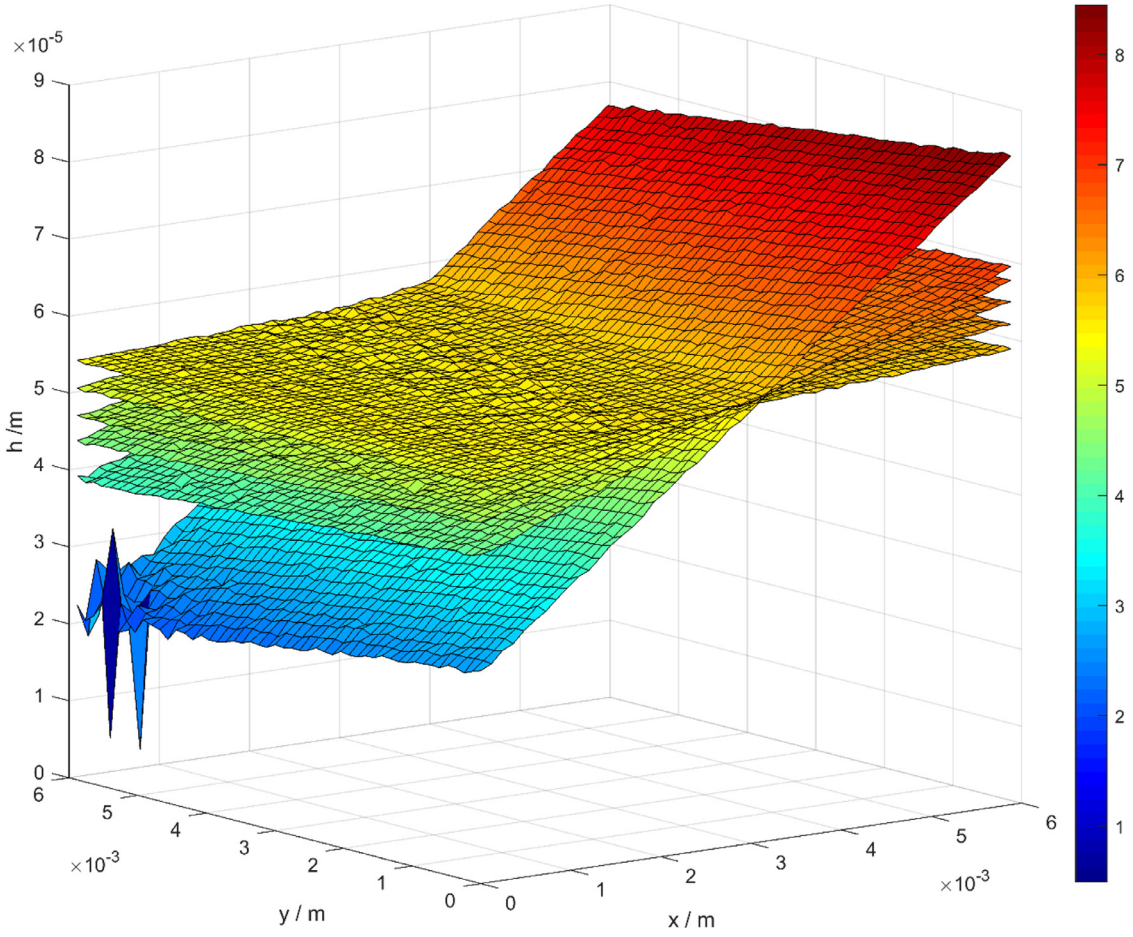


**Fig. 14.** Measured height profiles for silver mirror at 0, 1, 2, 3, 4, 5, and 10 mrad tilt angle when the mirror is at 50 μm from the ZDL.

within 0.14 mrad. Deviations between the requested and the measured tilt angle are larger at up to 0.6 mrad, however the tilt stage is under open loop control so there is no independent verification of the actual tilt angle achieved. Although the errors increase at and above $\theta = 10$ mrad, the results demonstrate that the pinhole-array based system is able to measure surfaces at angles of up to 15 mrad, which is 50% more than the upper theoretical limit on surface tilt angle, $\theta_m^{(M)}$, as calculated in Section 2.4 for a microlens-array based system.

## 5. Conclusions

An improved hyperspectral interferometry system has been developed, and its performance on optically smooth, stepped and tilted surfaces has been explored in this paper. The new system uses an array of pinholes at the input of an imaging spectrometer to separate spatial and spectral information on a large format photodetector array. 2500 channels can be measured simultaneously, which more than doubles the throughput of the previously described system based on a microlens array and corresponds to a pixel utilization greater than 50%. Using a pinhole array solves the problem of wavefront separation at the pupil plane which is present in the microlens array based system, thus allowing a tilt angle acceptance of ±33.3 mrad without loss of modulation. A pinhole array of 50 × 50 pinholes with a diameter of 10 μm and a pitch of 120 μm allows coverage of an area of 5.88 × 5.88 $mm^2$ with a maximum unambiguous height range of 825 μm. The use of phase information to calculate surface profile, as opposed to the usual Fourier peak location method, was investigated in an HSI system for the first time. Although systematic errors were significant, random errors were reduced by over an order of magnitude, to values below 10 nm for a flat mirror.

## Funding

Funding for this project was provided by the EPSRC Centre for Doctoral Training in Embedded Intelligence (EP/L014998/1), EPSRC Future Metrology Hub (EP/P006930/1) and by Renishaw Plc.

## Acknowledgments

The authors gratefully acknowledge useful discussions with David McKendrick and Nick Weston, Renishaw Plc, and financial support from Renishaw, the EPSRC Centre for Doctoral Training in Embedded Intelligence and the EPSRC Future Metrology Hub.

## References

[1] Jalili N, Laxminarayana K. A review of atomic force microscopy imaging systems: application to molecular metrology and biological sciences. Mechatronics 2004;14(8):907–45.
[2] Pecheva E, et al. White light scanning interferometry adapted for large-area optical analysis of thick and rough hydroxyapatite layers. Langmuir 2007;23(7):3912–18.
[3] Barker A, Syam W, Leach R. Measurement noise of a coherence scanning interferometer in an industrial environment. 31th ASPE annual meeting Portlan , Oregon, USA; 2016.
[4] . Geometrical product specifications (GPS) – Surface texture: areal – Part 604: nominal characteristics of non-contact (coherence scanning interferometry) instruments. International Organization for Standardization; 2013. p. 41.
[5] de Groot P. Principles of interference microscopy for the measurement of surface topography. Advances in Optics and Photonics 2015;7(1):1–65.
[6] Schwider J, Zhou L. Dispersive interferometric profilometer. Optics Letters 1994;19(13):995–7.

[7] Huntley JM, Widjanarko T, Ruiz PD. Hyperspectral interferometry for single-shot absolute measurement of two-dimensional optical path distributions. Measurement Science and Technology 2010;21(7):075304.
[8] Widjanarko T, Huntley JM, Ruiz PD. Single-shot profilometry of rough surfaces using hyperspectral interferometry. Optics Letters 2012;37(3):350–2.
[9] Ruiz PD, Huntley JM. Single-shot areal profilometry using hyperspectral interferometry with a microlens array. Opt Express 2017;25(8):8801–15.
[10] Graulig C, Kanka M, Riesenberg R. Phase shifting technique for extended inline holographic microscopy with a pinhole array. Optics Express 2012;20(20):22383–90.
[11] Nakano A. Spinning-disk confocal microscopy – a cutting-edge tool for imaging of membrane traffic. Cell Struct Funct 2002;27(5):349–55.
[12] de Groot P, Deck L. Three-dimensional imaging by sub-Nyquist sampling of white–light interferograms. Optics Letters 1993;18(17):1462–4.
[13] Huntley JM, et al. Absolute distance from phase in spectral interferometry Opt. express (to be submitted Apr. 2019); 2019.

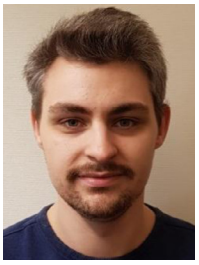

**Tobias V. Reichold** received a MEng in Aerospace Engineering from the University of Leicester in 2015. The same year he began his PhD in single-shot hyperspectral interferometry at Loughborough University with the Centre of Doctoral Training in Embedded Intelligence CDT-EI. He currently holds the associate member status with the Institute of Mechanical Engineers IMechE. His research interests include surface profilometry, depth-resolved measurements, optical system design and miniaturization.

**Dr. Pablo D. Ruiz** received his BA in Physics in 1996 from the National University of Salta and PhD in 2002 from the Rosario Institute of Physics at the National University of Rosario, Argentina. He joined Loughborough University in 2002, where he currently holds a readership in Applied Optics. His research interests include interferometry, lidar, speckle metrology, optical coherence tomography, synthetic aperture interferometry, elastography and the application of optical methods in experimental mechanics.

**Prof. Jonathan M. Huntley** has been involved in the development and application of full-field optical techniques for over 30 years, including 11 years at the Cavendish Laboratory, Cambridge. Appointed Professor of Applied Mechanics at Loughborough in 1999, he has published over 110 journal papers, two granted patent families, is a Fellow of the Institute of Physics, and was awarded the Institute of Physics Paterson Medal and Prize in 2005.